surfaces

MDPI

Article

Potential Driven Non-Reactive Phase Transitions of Ordered Porphyrin Molecules on Iodine-Modified Au(100): An Electrochemical Scanning Tunneling Microscopy (EC-STM) Study

Tomasz Kosmala [1,2,*], Matías Blanco [1], Gaetano Granozzi [1] and Klaus Wandelt [2,3,*]

1 Department of Chemical Sciences and INSTM Unit, University of Padova, Via F. Marzolo 1, 35131 Padova, Italy; matias.blancofernandez@unipd.it (M.B.); gaetano.granozzi@unipd.it (G.G.)
2 Institute of Physical and Theoretical Chemistry, Bonn University, Wegeler-Strasse 12, D-53115 Bonn, Germany
3 Institute of Experimental Physics, Plaza Maxa Borna 9, 50-204 Wroclaw, Poland
* Correspondence: tomasz.kosmala@unipd.it (T.K.); k.wandelt@uni-bonn.de (K.W.)

Received: 3 July 2018; Accepted: 24 July 2018; Published: 25 July 2018

Abstract: The modelling of long-range ordered nanostructures is still a major issue for the scientific community. In this work, the self-assembly of redox-active tetra(*N*-methyl-4-pyridyl)-porphyrin cations (H_2TMPyP) on an iodine-modified Au(100) electrode surface has been studied by means of Cyclic Voltammetry (CV) and in-situ Electrochemical Scanning Tunneling Microscopy (EC-STM) with submolecular resolution. While the CV measurements enable conclusions about the charge state of the organic species, in particular, the potentio-dynamic in situ STM results provide new insights into the self-assembly phenomena at the solid-liquid interface. In this work, we concentrate on the regime of positive electrode potentials in which the adsorbed molecules are not reduced yet. In this potential regime, the spontaneous adsorption of the H_2TMPyP molecules on the anion precovered surface yields the formation of up to five different potential-dependent long-range ordered porphyrin phases. Potentio-dynamic STM measurements, as a function of the applied electrode potential, show that the existing ordered phases are the result of a combination of van der Waals and electrostatic interactions.

Keywords: porphyrins; self-assembly; surface nanostructures; in situ EC-STM; metal-electrolyte interface; potential-dependent structures; combined non-covalent control

1. Introduction

One of the major challenges in the development of supramolecular nanoarchitectures is to find effective and flexible methods in order to create nanostructures with long range order [1,2]. In recent years, supramolecular self-assembly attracted much attention by the scientific community: as a well-known bottom-up method, molecular self-assembly on surfaces is a simple and fast tool to build nanoscale structures, which can be readily tuned by the on-purpose synthesis of appropriate molecular building blocks, and, thereby, the design of the noncovalent interactions between the molecules and the substrate and the molecules themselves [3–7]. Moreover, to direct the ordering process of the supramolecular nanoarchitectures, one can take advantage of well-defined single crystal surfaces, which can serve as electronic and/or geometric templates due to the operation of specific adsorbate-substrate interactions. In this case, the resulting supramolecular structures may be dictated by the symmetry and periodicity of the substrate surface. In contrast to the assembly of supramolecular architectures in three-dimensional (3D) bulk environments, e.g., solutions, where assembly is governed only by specific and directional intermolecular interactions, a complex interplay between

adsorbate-adsorbate and adsorbate-substrate interactions controls the two-dimensional (2D)-phase formation behavior when surfaces come into play [8–10]. Furthermore, if these molecular building-blocks are deposited electrochemically in the form of ions, the electrochemical (EC) potential becomes a very useful control parameter, which allows for influencing the self-assembly process [11–13]. In the end, the capability of many organic molecules to spontaneously self-assemble into molecular monolayers on suitable solid substrates may lead to functional surfaces with broad applications in electronic devices with nanometer dimensions, "green energy" catalysts, or novel light-stimulated sensors [14,15].

Among other examples, porphyrins, due to the wide range of potential applications of this class of molecules, e.g., in cancer therapy [16,17], catalysis [18,19], and sensing [20,21], have become prototypical systems for the fabrication and design of supramolecular nanoarchitectures and the characterization of their formation mechanism [22,23]. As an example from the point of applications, tetra (*N*-methyl-4-pyridyl)-porphyrin *p*-tolylsulfonate molecules (H_2TMPyP, Figure 1) were proven to be good sensors for the detection of benzene and heavy metal ions (Hg^{2+}, Pb^{2+}, Cd^{2+}) in water [24]. From self assembling studies in ultra-high-vacuum (UHV), it is known that adsorbed porphyrins on bare metal surfaces lie flat due to their large conjugated π-electron systems, which have the tendency to maximize the π-bonding with the surface [25]. In the EC environment, however, it is expected that electrostatic interactions of the porphyrin cations with the charged metallic electrode surface will also have a strong influence. Moreover, when compared to an adsorbed porphyrin layer in UHV, the electrode surface in contact with an electrolyte may be modified by the presence of specifically adsorbed anions from the supporting electrolyte. The influence of these preadsorbed anions on the deposition of organic cations depends obviously very much on their charge state. In the present work the surface is modified by iodide anions, which are known to be almost uncharged, so that, the iodine-porphyrin interactions are mainly dispersive in nature, i.e., of van der Waals type [26–28]. Actually, self-assembly of H_2TMPyP has been already investigated on various iodine modified metallic surfaces, such as Au(111) [26,27], Pt(100), Ag(111) [29,30], Cu(111), and Cu(100) [11,28]. To the best of our knowledge, studies on the self-assembly of porphyrins on the iodine precovered Au(100) surface have not been reported yet. Here, we present the results of combined Cyclic Voltammetry (CV) and in situ Scanning Tunneling Microscopy (STM) investigations. While the CV measurements enable conclusions about the charge state of the adsorbed molecules, in particular, potentio-dynamic STM measurements provide insight into their structural self-assembly on the surface. In this work, we concentrate on the "non-reactive" potential regime, i.e., the potential regime in which the molecules retain their oxidation state upon adsorption. Already in this restricted regime at positive potentials up to five different potential-dependent long-range ordered phases of the H_2TMPyP molecules are found on the iodine-modified Au(100) electrode. The different observed phases are thus not a consequence of the variation of the redox-state of the molecules themselves, but only of the electrode potential (and the concomitant change in iodine coverage). The potential induced modification of the non-covalent interactions, namely van der Waals and electrostatic forces between the assembled molecules and the substrate, is the only driving force for the observed phase transitions between the five porphyrin structures in their constant oxidized form ($[H_2TMPyP(0)]^{+4}$).

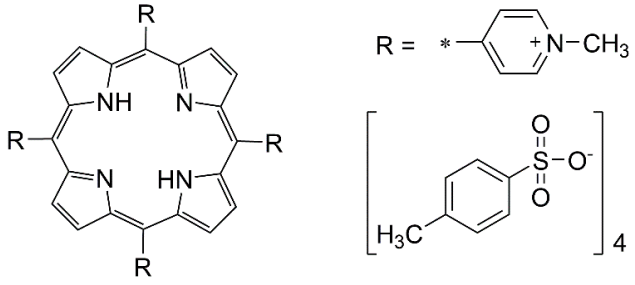

Figure 1. H_2TMPyP molecular structure.

2. Materials and Methods

The results that are presented in this work were carried out using a home build in-situ EC scanning tunneling microscope at constant current mode described in detail by Wilms et al. [31]. All of the electrolytes were prepared by using deionized water from a Millipore®-Pure (Merck, Burlington, MA, USA) water system (with a specific resistance of 18 MΩ·cm and a residual amount of organic impurities in the ppb regime) and purged with suprapure argon gas for several hours before use. Chemicals used (purchased from Sigma-Aldrich, Saint Louis, MO, USA) have the highest commercially available quality level and were used without further purification. The STM tips were electrochemically etched from a 0.25 mm tungsten wire in 2 M KOH solution and subsequently rinsed with high purity water, dried, and coated by passing the tip through a drop of hot glue.

The Au(100) electrode (MaTeck Company, Juelich, Germany) was annealed before each measurement in order to clean and smooth the surface. For this purpose, the sample was located on a Ceran® plate and was annealed by a butane-oxygen gas flame for three minutes up to faint red glow (600–700 °C). Subsequently, the crystal was cooled down to room temperature (about 15 min) in an atmosphere of argon. Then, it was heated again to a red glow and cooled for six minutes. To prevent the re-contamination of the surface after the cleaning procedure, the crystal was covered by a protective drop of Millipore®-water and immediately mounted into the EC cell of the EC-STM.

Cyclic Voltammetry (CV) and STM measurements were first performed in the pure supporting aqueous 5 mM H_2SO_4 + 1 mM KI electrolyte. In this electrolyte, the iodine-modified Au(100)-surface shows several phase transitions, starting from a $\left(\sqrt{2} \times p\sqrt{2}\right)$ at negative potentials, over a $\left(\sqrt{2} \times 2\sqrt{2}\right)$ to a *pseudo-hex-rot* structure at positive potentials. Both the $\left(\sqrt{2} \times p\sqrt{2}\right)$ and the *pseudo-hex-rot* structure exhibit the phenomenon of reversible electro-compression [32–34]. For the adsorption experiments the supporting electrolyte in the cell was replaced by a solution containing sulfate, iodide, and H_2TMPyP porphyrin molecules (5 mM H_2SO_4 + 1 mM KI + 0.01 mM H_2TMPyP). The potential of the gold electrode was controlled with respect to a Pt/PtI quasi-reference electrode, whose potential is related to that of the reversible hydrogen electrode (RHE) by the relation: RHE = Pt/PtI + 580 mV.

The base vectors that were employed for the description of the ordered structures of the various in the Results and Discussion section follow the common code:

- $\vec{a_x}$ for the base vector of the Au(100) lattice (x = 1,2);
- $\vec{b_x}$ and $\vec{b'_x}$ for the base vectors of the iodine lattice (x = 1,2); and,
- $\vec{c_x}$, $\vec{d_x}$, $\vec{e_x}$, $\vec{f_x}$ and $\vec{g_x}$ for the base vectors of the porphyrin phases P_I–P_V (x = 1,2).

3. Results and Discussion

3.1. Cyclic Voltammetry and H_2TMPyP Structures

The structural investigations of the organic layers that are presented in this work have exclusively been carried out under "non-reactive" conditions, i.e., in the regime where no redox-processes of the porphyrin molecules take place, as revealed by the survey cyclic voltammogram (CV) of the overall system shown in Figure 2a (see the red indicated region in Figure 2a). The first surface reduction/re-oxidation step of the molecules is indicated by the peak couple P_{red}/P_{ox}, as verified by the following EC-STM measurements. Also, the adsorption/desorption of the iodine anions is marked in the CV traces. As can be seen, the iodine desorption and the hydrogen evolution reaction (HER) are retarded due to the presence of the molecules. Hence, we focus and place emphasis exclusively on the structures of the $[H_2TMPyP(0)]^{4+}$ adlayer and their changes merely driven by changes of the electrode potential on the positive side of P_{red}/P_{ox}.

It is well known that iodide anions adsorb specifically on the Au(100) surface, and even low coverages stabilize the unreconstructed Au(100)(1 × 1) structure of the substrate. At high coverages

the iodide anions form highly ordered layers, whose structure is potential dependent in terms of electro-compression or electro-expansion [32–34]. However, within the electrode potential range examined here, iodide forms a commensurate *pseudo-hex-rot* iodine structure on Au(100) [32–34], and our results indicate a *pseudo-hex-rot* iodine structure that is rotated by about 2.6° with respect to the substrate $\sqrt{2}$ direction (Figure 2b), and consequently exhibits a periodic variation of the iodine binding sites, resulting in the observed height, i.e., brightness, modulation. A ball model of this phase acquired at an electrode potential of −150 mV vs. Pt/PtI is shown in Figure 2c, and it includes the unit cell.

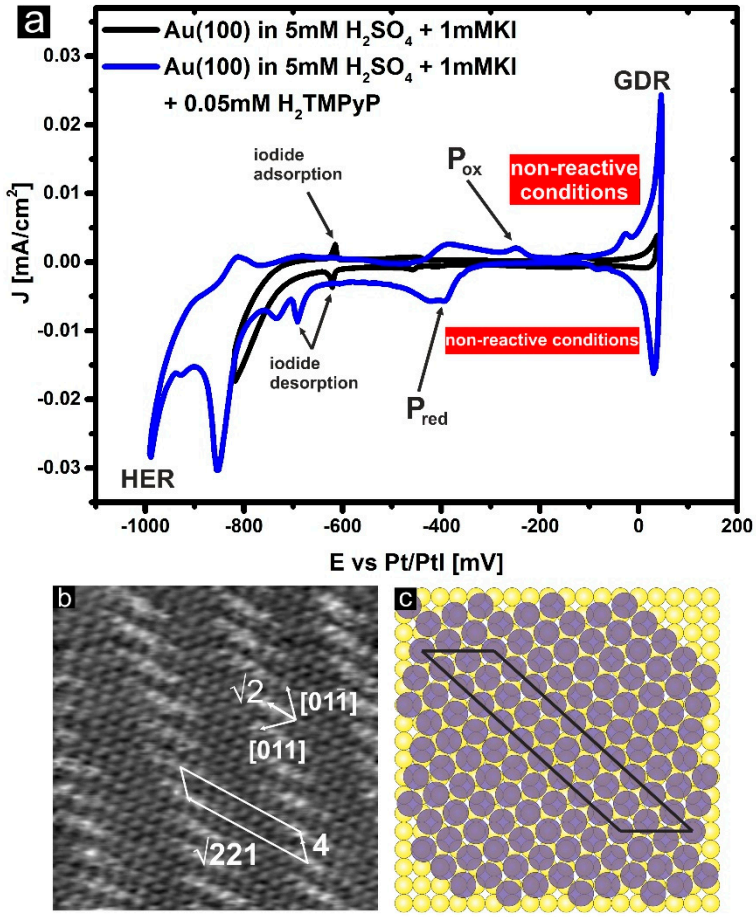

Figure 2. (**a**) Cyclic voltammograms of the Au(100) surface in 5 mM H_2SO_4 + 1 mM KI electrolyte solution (black curve) and in the H_2TMPyP containing electrolyte (blue curve, 5 mM H_2SO_4 + 1 mM KI + 0.05 mM H_2TMPyP), dE/dt = 10 mV·s^{-1}; GDR = gold dissolution reaction, HER = hydrogen evolution reaction, and the red bars indicate *non-reactive* regimes; (**b**) high-resolution in-situ Scanning Tunneling Microscopy (STM) image of the *pseudo-hex-rot* iodine structure obtained from a Au(100) surface in 5 mM H_2SO_4 + 1 mM KI solution; image parameters: 13.73 nm × 13.73 nm, I_t = 1 nA, U_b = −93 mV, E = −150 mV vs. Pt/PtI; (**c**) ball-model of the (4 × $\sqrt{221}$) iodine structure shown in (**b**).

Exposure of this iodine-modified Au(100) surface to the H_2TMPyP molecules containing 1 mM KI + 5 mM H_2SO_4 solution at potentials between the oxidative gold dissolution reaction (GDR) and the first reduction step of the porphyrin species (P_{red}) leads to spontaneous adsorption and the subsequent lateral ordering of H_2TMPyP molecules at the surface. The solution contains actually $[H_2TMPyP]^{4+}$ cations, but for the sake of ease we simply refer to H_2TMPyP molecules throughout this paper. The accompanying p-tolylsulfonate- as well as the SO_4^{2-}-anions from the supporting electrolyte adsorb weaker than iodide anions and therefore do not displace the latter [34].

Figure 3a presents a highly ordered layer of H_2TMPyP at an electrode potential −200 mV vs. Pt/PtI. Each bright dot represents one porphyrin molecule. Close-ups of this layer (Figure 3b–d) reveal that the molecules are self-assembled into differently ordered domains of molecular rows covering the atomically flat terraces. In addition, step edges (panel a) are oriented parallel to and decorated by molecular rows (see white and yellow lines in Figure 3a). A careful examination of Figure 3a–d clearly indicates the coexistence of five different porphyrin phases (P_I, P_{II}, P_{III}, P_{IV}, and P_V). Within each phase, translational domains (Figure 3b,c molecular rows of the domain highlighted by yellow solid lines) and the respective domain boundaries between them (Figure 3b,c yellow dashed lines) are observed.

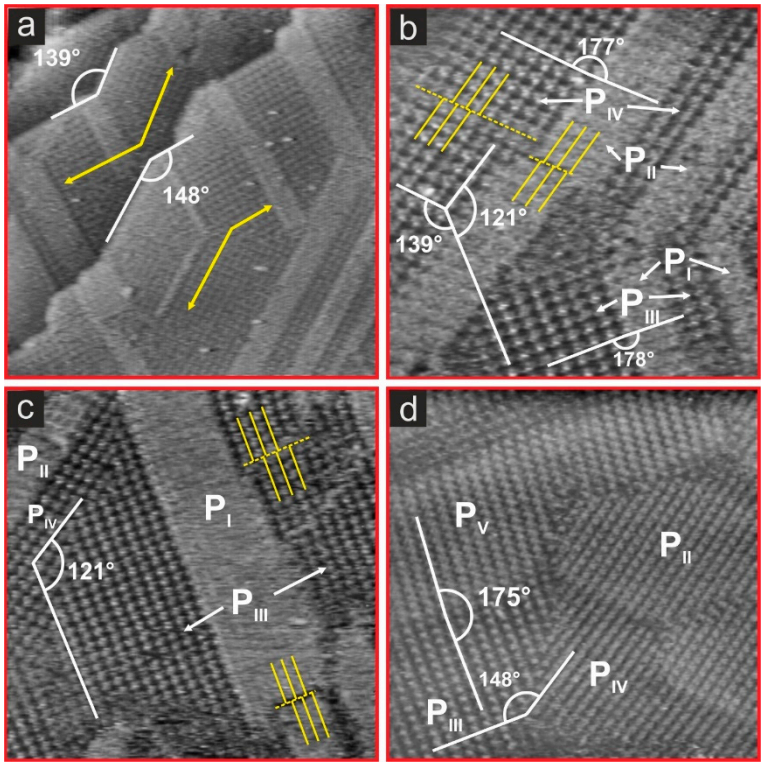

Figure 3. Electrochemical Scanning Tunneling Microscopy (EC-STM) images of self-assembled H_2TMPyP molecules on an iodine-modified Au(100) electrode in the *non-reactive* regime. P_I–P_V refer to structurally different phases. (**a**) 83.55 nm × 83.55 nm, I_t = 1 nA, U_b = −320 mV, E = −200 mV vs. Pt/PtI; (**b**) 42.35 nm × 42.35 nm, I_t = 1 nA, U_b = −472 mV, E = −200 mV vs. Pt/PtI; (**c**) 56.47 nm × 56.47 nm, I_t = 1 nA, U_b = −491 mV, E= −200 mV vs. Pt/PtI; (**d**) 56.47 nm × 56.47 nm, I_t = 1 nA, U_b = −303 mV, E = −200 mV vs. Pt/PtI.

In order to shed light on these porphyrin phases, STM images with atomic resolution were registered (Figure 4a–d). These images clearly reveal that the organic macrocycles are lying flat on the substrate due to their large molecular π-electron system and the tendency to maximize the π-bonding to the surface, as reported before [11,26–28]. The STM images show that each flat-lying porphyrin molecule can be recognized as a square-shaped motif with the characteristic four additional lobes placed at the four corners of each square (see inset and blue molecules in Figure 4a). The center-to-center distance measured diagonally across one molecule between the corner spots is 1.2 ± 0.1 nm, which is consistent with the distance between two diagonally located pyridinium units [26]. Furthermore, a detailed analysis of images, like in Figure 4, yields the characteristic lattice parameters, like vectors, rotation angles, molecules per unit cell, and surface coverage of the five different phases (P_I–P_V). These structural data are collected in Table 1.

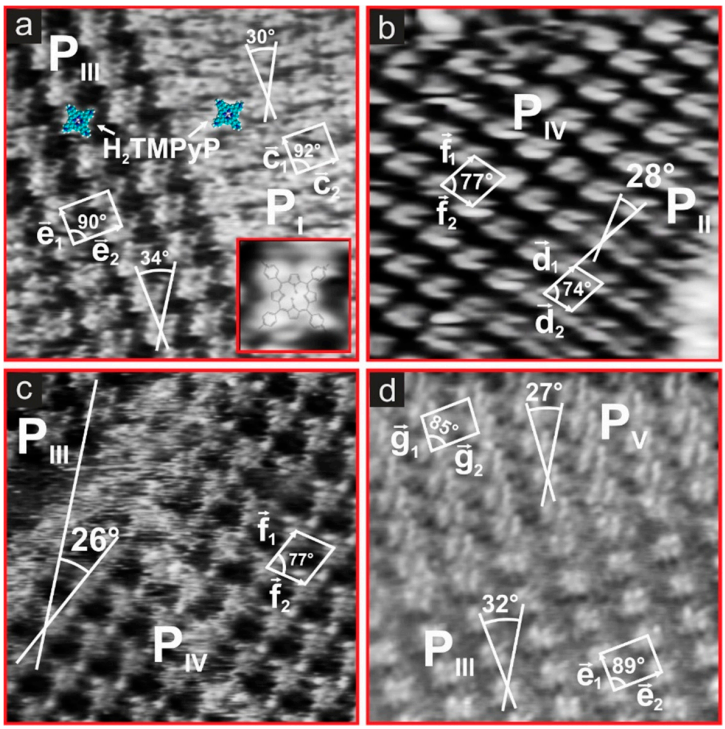

Figure 4. High-resolution EC-STM images of the ordered H_2TMPyP adlayer on an iodine-modified Au(100) electrode in the *non-reactive* regime. (**a**) 14.12 nm × 14.12 nm, I_t = 1 nA, U_b = −472 mV, E = −200 mV vs. Pt/PtI. Size of inset: 1.94 nm × 1.94 nm; (**b**) 14.15 nm × 14.15 nm, I_t = 1 nA, U_b = −291 mV, E = −200 mV vs. Pt/PtI; (**c**) 14.12 nm × 14.12 nm, I_t = 1 nA, U_b = −472 mV, E = −200 mV vs. Pt/PtI; (**d**) 14.12 nm × 14.12 nm, I_t = 1 nA, U_b = −303 mV, E= −200 mV vs. Pt/PtI.

Table 1. Structural data of the five different self-assembled, potential dependent H_2TMPyP structures P_I–P_V on an iodine-modified Au(100) electrode surface as detected by in situ STM in the non-reactive potential regime.

Parameter	P_I	P_{II}	P_{III}	P_{IV}	P_V
lattice constants [±0.05 nm]	c_1 = 1.61 c_2 = 1.80	d_1= 1.94 d_2 = 1.56	e_1 = 1.61 e_2 = 2.06	f_1 = 1.94 f_2 = 1.76	g_1 = 1.46 g_2 = 2.06
angle [±1°]	92°	74°	89°	77°	85°
molecule rotation [α ±1°]	+30° vs. $\vec{c_1}$	−28° vs. $\vec{d_1}$	+32° vs. $\vec{e_1}$	+26° vs. $\vec{f_1}$	+27° vs. $\vec{g_1}$
surface concentration [molecules/cm^2]	3.453 × 10^{13}	3.437 × 10^{13}	3.016 × 10^{13}	3.014 × 10^{13}	3.333 × 10^{13}

Based on these experimental results of the symmetry and orientation of the H_2TMPyP molecules, in Figure 5 we propose a schematic model of the ordered H_2TMPyP porphyrin molecules for each phase. It is important to emphasize that the value of the surface coverage of phase P_V lies in the middle of those of the other phases. Furthermore, P_V was observed rather rarely in comparison to phases P_I–P_{IV}: it only appears when the adsorption process started at an electrode potential of ca. −200 mV vs. Pt/PtI, and it vanishes altogether at those potential values where the phases P_I–P_{IV} were observed within more extended regimes of the electrode potential (*vide infra*). This suggests that P_v is less stable than P_I–P_{IV} and it is observable only under specific conditions in this very narrow electrode potential window, e.g., after adsorption at −200 mV vs. Pt/PtI and within a narrow range of electrode potential.

As mentioned previously, within the potential window investigated here, the porphyrin molecules do not undergo any redox process. Hence, the observed phase transitions are *not* triggered by a

variation of the chemical state of the porphyrin due to an electron transfer process; but it can only be traced back to changes of the interactions between the porphyrin molecules and the substrate [11,35,36].

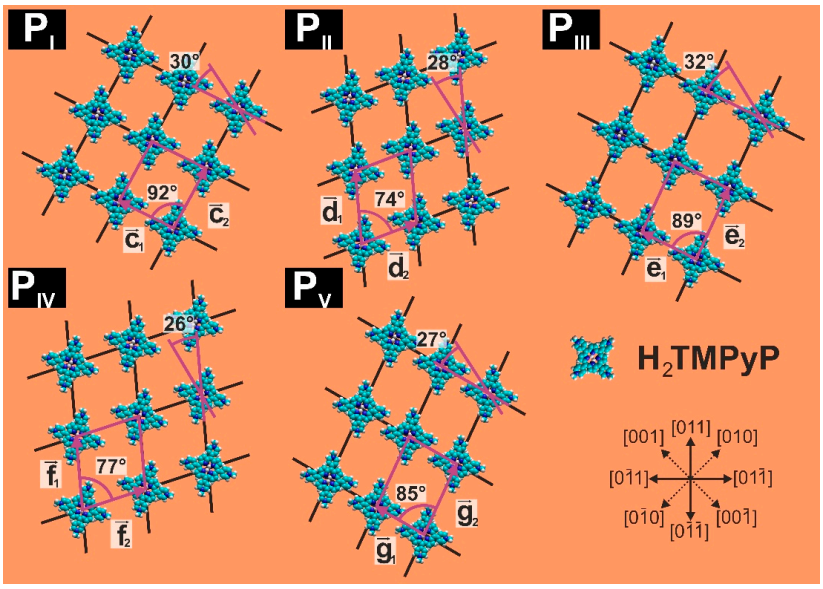

Figure 5. Schematic models of the five ordered H_2TMPyP molecular phases in the *non-reactive* regime on I/Au(100), with the denoted vectors of the unit cells, the angles between them, and the angle of rotation of individual molecules off the molecular row direction (see Table 1).

3.2. Electrode Potential Stability of H_2TMPyP Phases on I/Au(100)

In order to check the stability and existence of phases P_I–P_V as a function of potential, and whether there is a competition (i.e., a difference in stability) between them expressed by their different equilibrium coverages, we also performed potentio-dynamic STM studies. These potentio-dynamic STM measurements were started at −200 mV vs. Pt/PtI (see Figure 2) with a highly ordered porphyrin layer comprising the first four phases P_I–P_{IV}, as shown in Figure 6a). The following images in panels b–i of Figure 6 are a selection out of a series of 170 successive images and are taken at the indicated potentials. They are largely registered at the same surface position (indicated by the red arrow in Figure 6a–i). However, due to thermal drift this marker slowly drifted out of the scanned area so that the last three images 6j–l were recorded around a new point of the same area (marked with a light blue arrow). From the starting point (Figure 6a reflects the very initial state, which was allowed to equilibrated for 210 s before the series of 170 images was started with Figure 6b), the electrode potential was first scanned in the cathodic direction. The areas covered by P_I and P_{II} are observed to shrink while those of P_{III} and P_{IV} start to grow. When the potential reaches −300 mV vs. Pt/PtI, within less than 5 min, the phases P_I and P_{II} are finally completely replaced by P_{III} and P_{IV} (see Figure 6c,d). Moreover, new bright spots appear in the images (see white arrows in Figure 6c), which represent the growth of a completely new ordered phase. A height profile measured along the short orange line in Figure 6d and shown in the inset yields a height difference between the bright spots and the dark region between them of around 0.3 nm. This value approximately matches the thickness of one flat lying porphyrin molecule [37].

These observations suggest that, when approaching the reactive regime (below −300 mV vs. Pt/PtI), the new bright spots represent adsorption of molecules in the second layer. This is supported by lowering of the electrode potential even further to −300 mV and −400 mV, which leads to an increase of the bi-layer coverage and the creation of new phases under these reactive conditions, named P_{VI} and P_{VII} (Figure 6d–f). Both monolayer phases P_{III} and P_{IV} phases are finally completely replaced by the bi-layer when the potential reaches the maximum of peak P_{red} at −395 mV vs. Pt/PtI,

which represents the first reduction step of the porphyrin molecules. Thus, the appearance of the bi-layer in the STM images in coincidence with the first reduction peak in the CV clearly marks the cathodic limit of the *non-reactive* monolayer adsorption regime. The full analysis of the EC-STM data under reactive conditions will be the subject of a forthcoming paper. Here, we concentrate on changes on the surface upon sweeping the potential back into the positive direction. No changes where noticed until the electrode potential reached again −300 mV vs. Pt/PtI. At this potential, re-entering in the *non-reactive* regime, a disordering of the lateral structure at the domain boundaries as well as desorption of second layer porphyrin molecules starts to take place (see yellow arrows in Figure 6g). At the potential −250 mV vs. Pt/PtI (corresponding to the anodic peak P_{ox}) the second layer has almost completely disappeared, and at a potential of ca. −200 mV vs. Pt/PtI, represented by Figure 6i, phases P_I and P_{II} have reappeared on the surface. Changing the electrode potential even further in anodic direction leads to growth of P_I and P_{II} at the expense of P_{III} and P_{IV} (see Figure 6j,k), and finally a complete replacement of the latter two phases. Moreover, at a potential of −100 mV vs. Pt/PtI the GDR starts at the step-edges as revealed by the course of the step edge in Figure 6k. After reaching the electrode potential of −50 mV vs. Pt/PtI where the GDR proceeds very quickly (see Figure 6l), P_{II} completely disappears from the surface, while P_I is still clearly observable.

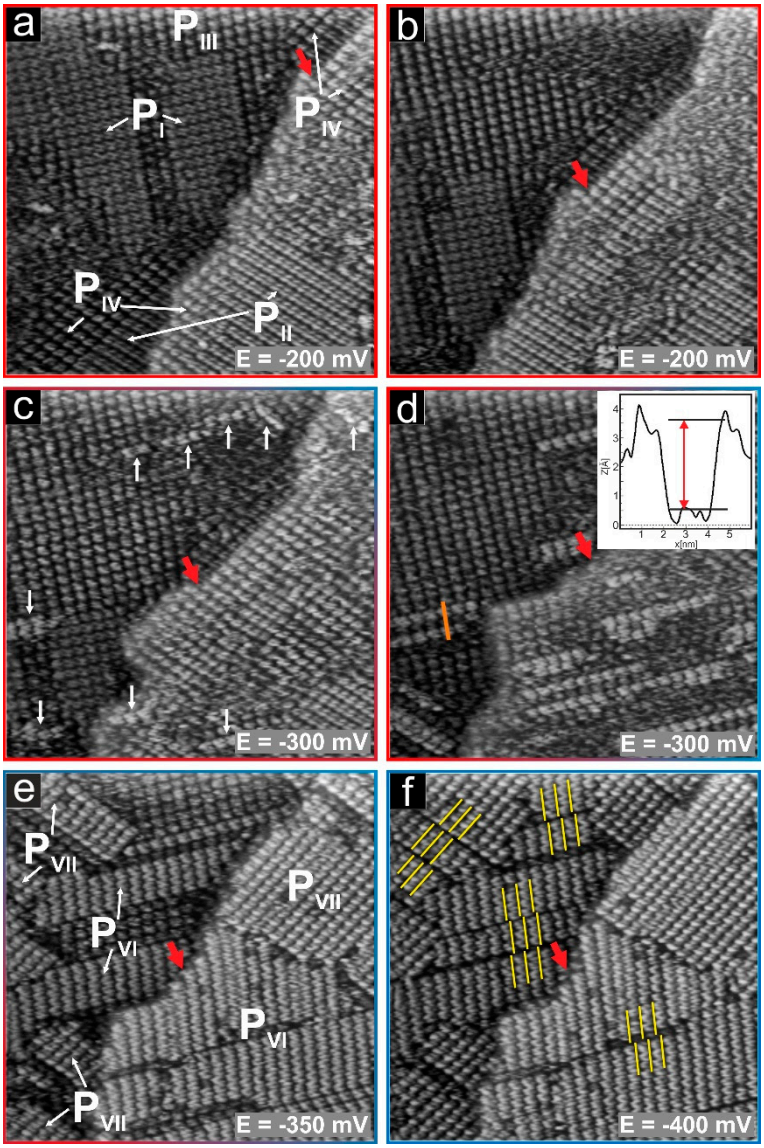

Figure 6. *Cont.*

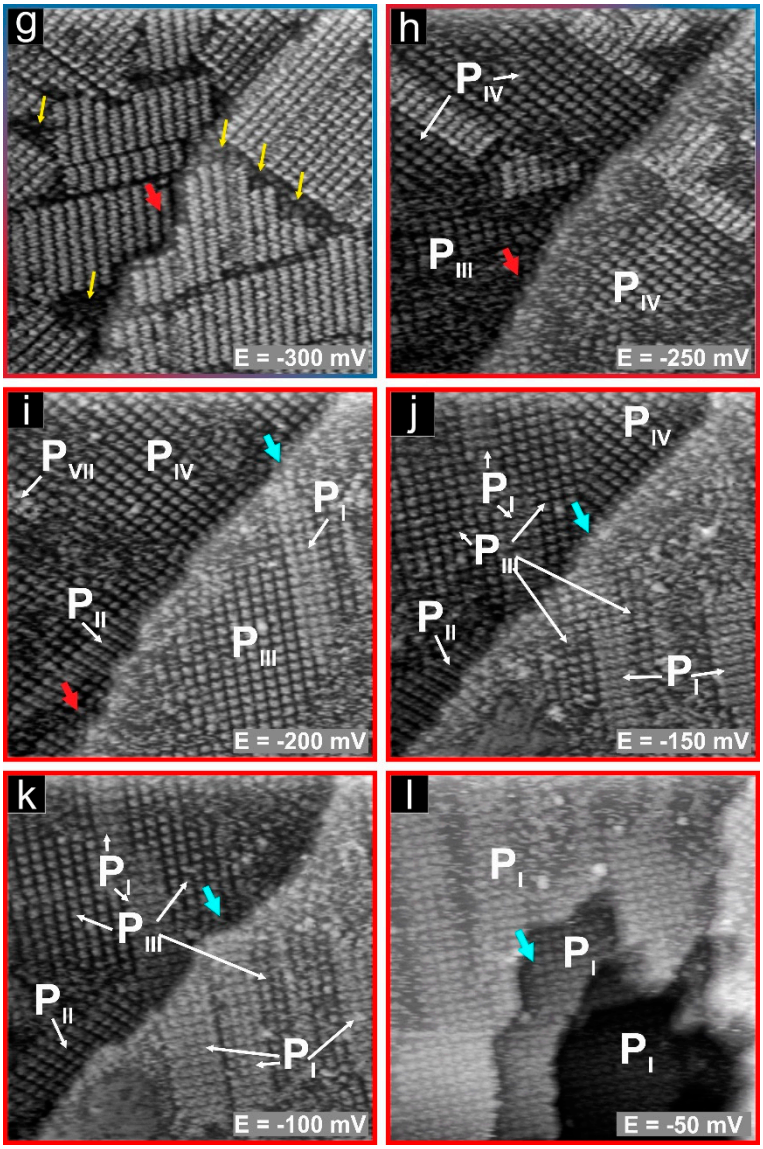

Figure 6. Potential induced phase transition of molecular H_2TMPyP adlayer on an I/Au(100) electrode surface, STM series: 50.32 nm × 50.32 nm; (**a**) I_t = 1 nA, U_b= −291 mV; (**b**) I_t = 1 nA, U_b = −267 mV; (**c**) I_t = 1 nA, U_b = −267 mV; (**d**) I_t = 1 nA, U_b = −267 mV; (**e**) I_t = 1 nA, U_b = −208 mV; (**f**) I_t = 1 nA, U_b = −208 Mv; (**g**) I_t = 1 nA, U_b = −208 mV; (**h**) I_t = 1 nA, U_b = −208 mV; (**i**) I_t = 1 nA, U_b = −250 mV; (**j**) I_t = 1 nA, U_b = −477 mV; (**k**) I_t = 1 nA, U_b = −461 mV; (**l**) I_t = 1 nA, U_b = −461 mV. For explanation of the different colored arrows see the text.

Figure 7 represents a diagram that indicates the stable potential and coexistence regimes of the five phases P_I–P_V. The above potentio-dynamic STM measurements reveal a competition between these phases, i.e., their relative stability as a function of electrode potential, as manifested by their different surface concentrations. Furthermore, from a correlation of the structural changes with the relative coverage of each phase, we arrive at a strict relationship between the potential regime of each phase and its surface concentration: according to Table 1, P_I has the highest surface density (3.453×10^{13} molecules/cm^2) and its existence regime is at the most positive potentials in comparison to all other phases. Next, P_{II} with a lower density (3.437×10^{13} molecules/cm^2) than P_I occurs at lower potentials. Finally, P_{III} and P_{IV} with the lowest surface concentrations among all five monolayer phases (of 3.016×10^{13} molecules/cm^2 and 3.006×10^{13} molecules/cm^2, respectively) have their existence regimes at the most negative potentials.

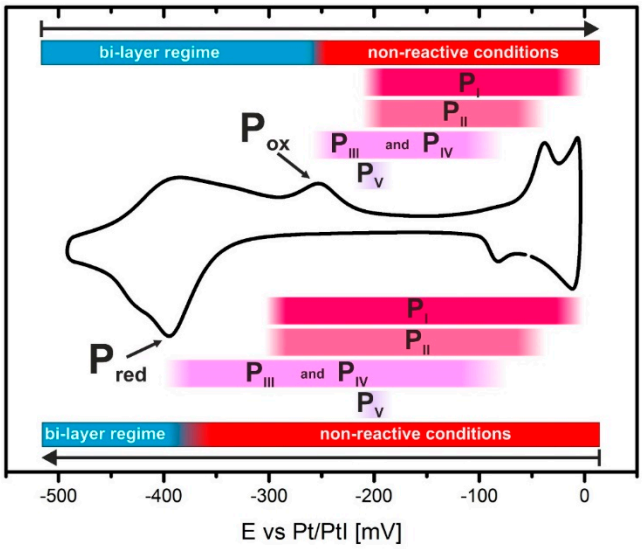

Figure 7. Diagram of the stability regimes of the P_I–P_V monolayer phases of adsorbed H_2TMPyP on an iodine-modified Au(100) electrode surface.

Therefore, in order to get more insights and to understand the relations between the applied electrode potential and the different surface concentration of each porphyrin phase, a set of STM images was taken, which provides a direct correlation between the structure of the different organic phases and that of the underlying iodine and gold lattice.

3.3. Substrate-Adlayer Structure Correlations

3.3.1. Phases P_I, P_{III}

Owing to the overlap of the existence regimes, it is possible to record a set of STM images that comprise both phases P_I and P_{III} (14.12 nm × 14.12 nm, Figure 8a,b and Figure 8d,e) within the same surface area. It is well known that by changing the tunneling conditions (namely tunneling bias) a resonant tunneling may be achieved [38,39]. At high bias voltage (e.g., $U_b = -416$ mV in Figure 8a, and $U_b = -472$ mV in the lower half part of Figure 8d), almost all electrons flow via resonant tunneling through quantized energy levels that are defined by the molecular orbitals or the band generated by the periodic arrangement of the molecules. Thus, tunneling through these states emphasizes the contribution of the organic molecules in the respective STM images. On the other hand, at lower bias voltage (e.g., $U_b = -9$ mV in the upper-left part of Figure 8d and left part of Figure 8e), the normal tunneling process dominates the tunneling current, where electrons tunnel through the potential well without interacting with the localized discrete molecular levels. Most importantly, in some cases at an intermediate bias voltage it is possible that both tunneling channels through the potential well and the localized discrete levels contribute to the image. Thus, images that are registered at this intermediate bias voltage comprise both types of features that can be associated either with the substrate or the adsorbate (see e.g., Figure 8b at $U_b = -13$ mV, and its Reverse Fast Fourier Transform (RFFT) in Figure 8c in which we can observe a signal from the porphyrin molecules as well as from the iodine lattice; and the upper-right part of Figure 8d and right part of Figure 8e at $U_b = -9$ mV, with the RFFT presented in Figure 8f performed on the right part of Figure 8e, in which contributions from gold and the porphyrin lattice are observed). Such images enable a direct correlation between the structure of the organic overlayer and that of the underlying iodine and the supporting gold lattice. Moreover, the *simultaneous* observation of features from both the molecules on the one hand, and iodine or gold underneath on the other hand, excludes that the observed bias dependence of the images is due to a physical removal of the molecules from the substrate by the tip at low bias voltages (Figure 8b,e).

This approach circumvents any problem with drift during image taking because both contributions, that from the molecules and that from the substrate, are included in the same image.

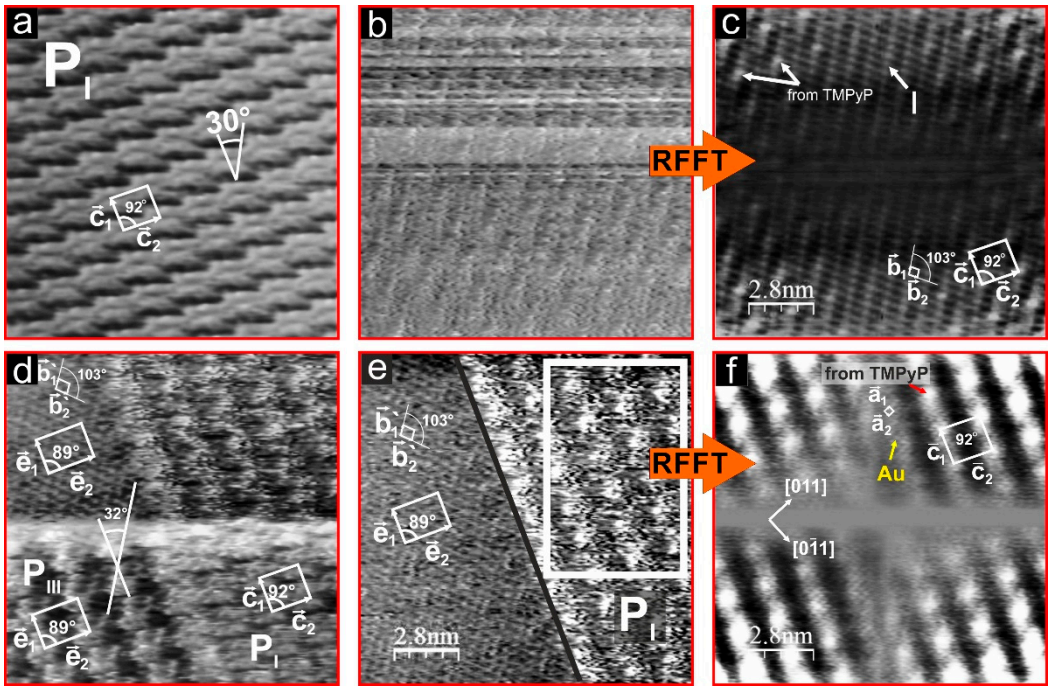

Figure 8. Correlation of the structures of the P_I and P_{III} monolayer phases of adsorbed H_2TMPyP molecules with the underlying iodine and gold layer, (**a**) P_I porphyrin layer at high tunneling bias, 14.12 nm × 14.12 nm, I_t = 1 nA, U_b = −416 mV, E = −200 mV vs. Pt/PtI; (**b**) Iodine layer underneath P_I at low tunneling bias, 14.12 nm × 14.12 nm, I_t = 1 nA, U_b = −13 mV, E = −200 mV vs. Pt/PtI; (**c**) a Reverse Fast Fourier Transform (RFFT) of the STM image (**b**); (**d**) upper part: Iodine layer underneath P_{III} at low tunneling bias: U_b = −9 mV, lower part: P_{III} porphyrin layer at high tunneling bias: U_b = −472 mV, 14.12 nm × 14.12 nm, I_t = 1 nA, E = −200 mV vs. Pt/PtI; (**e**) left part: Iodine layer underneath P_I at low tunneling bias: U_b = −9 mV, right part: combination of the Porphyrin layer and the substrate layer at low tunneling bias: U_b = −9 mV, 14.12 nm × 14.12 nm, I_t = 1 nA, E = −200 mV vs. Pt/PtI; (**f**) a Reverse Fast Fourier Transform (IFFT) of the left part of STM image (**e**).

Therefore, after close analysis and superimposition of the signals that are described above from the porphyrin-, iodine-, and Au-structure presented in Figure 8, it is possible to relate the structure of the molecular phases P_I and P_{III} to those of the iodine and the gold lattice underneath (see Figure 9). The iodine layer under both molecular phases was found to be a *pseudo-hex-rot* phase, but when considering that this iodine phase is electro-compressible (the iodine lattice becomes more compressed with increasing electrode potential), a differently compressed *pseudo-hex-rot* iodine phase should exist, and was actually found, under the two H_2TMPyP phases. With the set of images from Figure 8 in hand, it is thus possible to devise structure models of both phases P_I and P_{III}, and the corresponding data are summarized in Table 2.

Starting with P_I (Figure 9), we detect that in the direction of the vectors $\overline{b_1}$ every nineteenth and in the direction of the vector $\overline{b_2}$ every seventh iodine atom in the respective iodine row occupies a site on top of a gold atom. On the other hand, the molecular rows of the H_2TMPyP layer of P_I are not aligned with any high symmetry direction of the substrate, neither of the iodine lattice nor of the Au(100) surface. However, when considering the symmetry axis of individual molecules that are centred atop of an iodine atom, we observe that this axis is rotated by 30° off the row direction (see Table 1) and coincides with close-packed iodine rows running in the [0 7 35] direction of the substrate, respectively.

On the basis of this model the surface coverage of the porphyrin adlayer is calculated to be 0.0286 monolayers (ML) relative to the density of the *gold* layer.

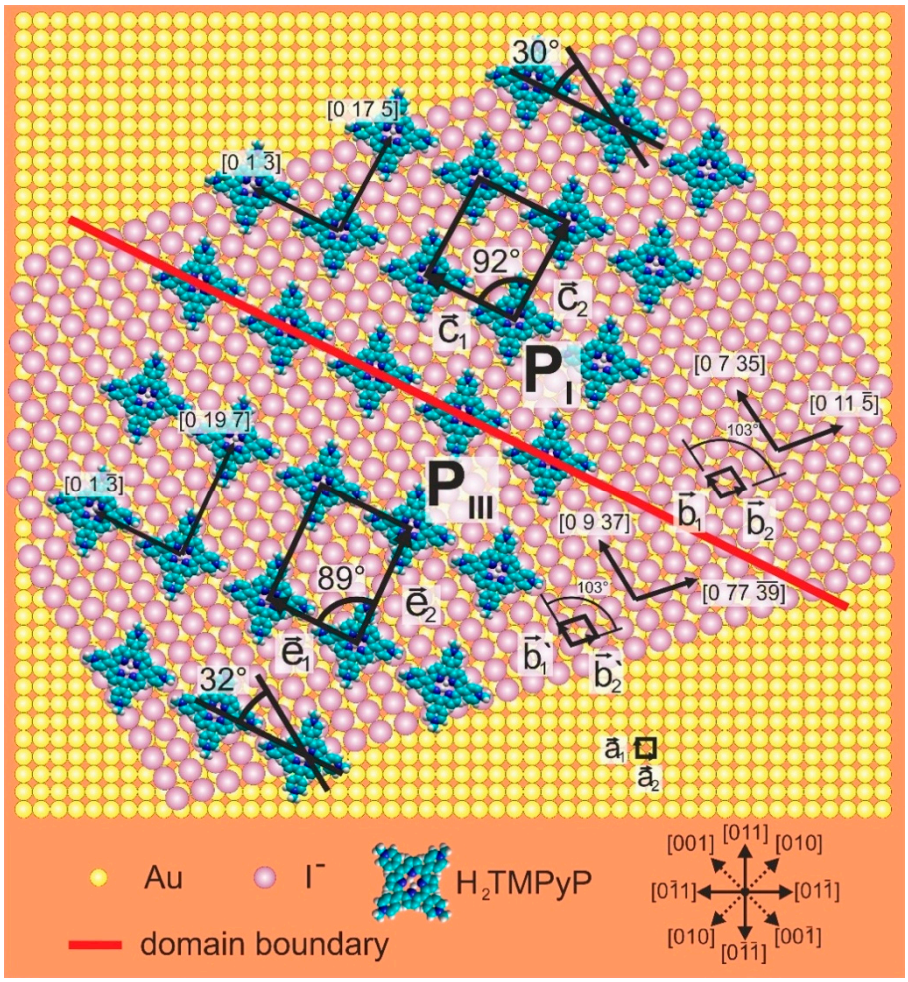

Figure 9. Structure models of the phases P_I and P_{III} on an iodine modified Au(100) surface.

In turn, for phase P_{III}, the iodine rows follow the direction of the vectors $\overline{b_1'}$ and $\overline{b_2'}$ instead, which in these directions leads to periodic atop binding sites of an iodine atom on a gold atom every twenty-first and forty-first iodine, respectively. The symmetry axis of individual molecules is rotated by 32° off the row direction (see Table 1), which coincides with the [0 9 37] substrate direction in this case. As a consequence, the iodine coverage under P_{III} (0.250 ML) is slightly lower than that under P_I (0.0286 ML). This lower iodine coverage is a consequence of the electro-expansion of the *pseudo-hex-rot* phase with decreasing electrode potential (0.52 ML under P_I vs. 0.50 ML under P_{III}, see Table 2).

Table 2. Data correlating the structures of the phases P_I, P_{III} and P_{IV} of self-assembled H_2TMPyP molecules on an iodine modified Au(100) electrode with those of the respective iodine layer and the Au(100) substrate underneath.

Parameter		P_I	P_{III}	P_{IV}
Au lattice parameters	vectors direction		$\overline{a_1} = [0\,1\,1]$ $\overline{a_2} = [0\,1\,\overline{1}]$	
	lattice constant		$a_1 = 0.289$ nm $a_2 = 0.289$ nm	
Iodine lattice parameters	vectors direction	$\overline{b_1} = [0\,7\,35]$ $\overline{b_2} = [0\,11\,\overline{5}]$	$\overline{b'_1} = [0\,9\,37]$ $\overline{b'_2} = [0\,77\,\overline{39}]$	$\overline{b'_1} = [0\,9\,37]$ $\overline{b'_2} = [0\,77\,\overline{39}]$
	lattice constant	$b_1 = 0.404$ nm $b_2 = 0.410$ nm	$b'_1 = 0.388$ nm $b'_2 = 0.439$ nm	$b'_1 = 0.388$ nm $b'_2 = 0.439$ nm
	Θ*	0.52 ML	0.50 ML	0.50 ML
	Matrix with respect to Au(100)	$\begin{pmatrix} \vec{b}_1 \\ \vec{b}_2 \end{pmatrix} = \begin{pmatrix} 3 & -2 \\ 3 & 8 \end{pmatrix} \begin{pmatrix} \vec{a}_1 \\ \vec{a}_2 \end{pmatrix}$	$\begin{pmatrix} \vec{b'}_1 \\ \vec{b'}_2 \end{pmatrix} = \begin{pmatrix} 11.5 & -7 \\ 19 & 58 \end{pmatrix} \begin{pmatrix} \vec{a}_1 \\ \vec{a}_2 \end{pmatrix}$	$\begin{pmatrix} \vec{b'}_1 \\ \vec{b'}_2 \end{pmatrix} = \begin{pmatrix} 11.5 & -7 \\ 19 & 58 \end{pmatrix} \begin{pmatrix} \vec{a}_1 \\ \vec{a}_2 \end{pmatrix}$
Porphyrins lattice parameters	vectors direction	$\overline{c_1} = [0\,1\,\overline{3}]$ $\overline{c_2} = [0\,17\,5]$	$\overline{e_1} = [0\,1\,\overline{3}]$ $\overline{e_2} = [0\,19\,7]$	$\overline{f_1} = [0\,61\,73]$ $\overline{f_2} = [0\,77\,\overline{39}]$
	Θ*	0.0286 ML	0.0250 ML	0.0250 ML
	Matrix with respect to iodine	$\begin{pmatrix} \vec{c}_1 \\ \vec{c}_2 \end{pmatrix} = \begin{pmatrix} 3 & -2 \\ 3 & 4 \end{pmatrix} \begin{pmatrix} \vec{b}_1 \\ \vec{b}_2 \end{pmatrix}$	$\begin{pmatrix} \vec{e}_1 \\ \vec{e}_2 \end{pmatrix} = \begin{pmatrix} 3 & -2 \\ 4 & 4 \end{pmatrix} \begin{pmatrix} \vec{b'}_1 \\ \vec{b'}_2 \end{pmatrix}$	$\begin{pmatrix} \vec{f}_1 \\ f_2 \end{pmatrix} = \begin{pmatrix} 5 & 2 \\ 0 & 4 \end{pmatrix} \begin{pmatrix} \vec{b'}_1 \\ \vec{b'}_2 \end{pmatrix}$
	Matrix with respect to Au(100)	$\begin{pmatrix} \vec{c}_1 \\ \vec{c}_2 \end{pmatrix} = \begin{pmatrix} 2.5 & -5 \\ 5.5 & 3 \end{pmatrix} \begin{pmatrix} \vec{a}_1 \\ \vec{a}_2 \end{pmatrix}$	$\begin{pmatrix} \vec{e}_1 \\ \vec{e}_2 \end{pmatrix} = \begin{pmatrix} 2.5 & -5 \\ 6.5 & 3 \end{pmatrix} \begin{pmatrix} \vec{a}_1 \\ \vec{a}_2 \end{pmatrix}$	$\begin{pmatrix} 5\vec{f}_1 \\ 5\vec{f}_2 \end{pmatrix} = \begin{pmatrix} 33.5 & -3 \\ 9.5 & 29 \end{pmatrix} \begin{pmatrix} \vec{a}_1 \\ \vec{a}_2 \end{pmatrix}$

* Surface coverage relative to the density of the gold layer.

Even though the determined differences in coverage of P_I and P_{III}, and, even more so, for the respective underlying iodine structures, may appear small, there is no doubt that they are real, because they are obtained from the coexisting phases in the same image of the same measurement.

Thus, P_I with a monolayer coverage of 0.0286 ML is situated on an iodine layer of coverage 0.52 ML, while P_{III} of coverage 0.0250 ML is found on an iodine underlayer of coverage 0.50 ML at lower potentials. In both phases, the direction of closest-packed molecular rows do not coincide with any high symmetry direction of neither the iodine nor the gold lattice underneath, but all of the molecules are centred on an iodine atom, and a symmetry axis of the molecules is aligned with the direction of a close-packed iodine row. Since both phases, P_I and P_{III}, occur within the *non-reactive* potential regime, and thus, retain their charge state, only differences in density and atomic arrangement of the iodine underlayer can be taken responsible for the differences between P_I and P_{III}, namely their different lattice parameters, and, in particular, their different atomic density.

Two arguments can be put forward to explain the higher coverage of P_I when compared to P_{III}. Firstly, the denser iodine anion layer underneath P_I (at higher potential) may correspond to a higher density of negative charge, which attracts more molecular cations. This argument, however, may not be valid because among the halides iodine binds most covalently, in particular the higher its coverage (at higher potentials) is. Iodine layers on noble metals, like Au or Pt, were found to be hydrophobic and almost uncharged [26]. The same conclusion was drawn from studies with iodine adsorption on Cu(100) [40,41]. Secondly, the denser the iodine layer the more effectively it screens the positive charge of the metal substrate, and thereby, reduces the electrostatic repulsion between the electrode and the molecular cations, and, instead, relatively strengthens van-der-Waals interactions between the molecules and the covalently bound iodine layer. Even though this dominance of van-der-Waals interactions has been favoured in the literature, our results indicate a combination of van-der-Waals and electrostatic forces. While the simultaneous increase of iodine- and H_2TMPyP-coverage with increasing electrode potential supports the notion of dominant van-der-Waals bonding of the molecules to the surface, the match of the symmetry direction of the individual molecules with the nearly rectangular iodine lattice underneath points to a contribution of electrostatic interactions, namely interlayer attraction between the positively charged *N*-methyl-4-pyridyl-ligands and the iodine lattice underneath, and intralayer repulsion between these ligands of the neighbouring molecules. Therefore, these latter electrostatic forces are actually responsible for the lateral order formation.

3.3.2. Phases P_{III}, P_{IV}

A similar comparative analysis can be done with phases P_{III} and P_{IV} based on images, as shown in Figure 10. According to Table 1, these two phases have essentially equal surface coverage and they are stable in the same potential range, as revealed by the potentio-dynamic STM measurements shown in Figure 6. In order to achieve a structural correlation between the molecular adlayer and the substrate underneath, we performed again bias dependent STM measurements (Figure 10a–c). As listed in Table 2, the *pseudo-hex-rot* structure of the iodine structure on the substrate is the same under both phases, and is described by the vectors $\overline{b_1'}$ and $\overline{b_2'}$ with directions of $[0\ 9\ 37]$ and $\left[0\ 77\ \overline{39}\right]$, respectively. In these directions, every twenty-first and forty-first iodine atom, respectively, occupies an atop binding site on a gold atom, and the iodine coverage is 0.50 ML (see Table 2). While the structural correlation of phase P_{III} with the iodine lattice underneath has already been described in the previous section, molecular rows of phase P_{IV} described by $\overline{f_1}$ and $\overline{f_2}$ with directions $[0\ 61\ 73]$ and $\left[0\ 77\ \overline{39}\right]$, respectively, run parallel to the iodine $\overline{b_2'}$ direction, but, interestingly, have the same orientation of the molecular symmetry axis as in P_{III} (coinciding with the $[0\ 9\ 37]$ direction of close packed iodine rows), as shown in Figure 11a. Therefore, if both unit cells of P_{III} (blue) and P_{IV} (red) are superimposed (as shown in Figure 11b) a new coincidence lattice ($\overline{S_1}$,$\overline{S_2}$) (green in Figure 11b) becomes apparent. The vector $\overline{S_1}$ of this structure is aligned with the densely packed iodine rows in the direction $\begin{bmatrix} 0 & 9 & 37 \end{bmatrix}$. The new (green) unit cell contains four molecules from P_{III} and four molecules from P_{IV}, plus one shared additional molecule (the green atom can be either blue or red in the model) every eleventh iodine atom underneath. The fact that both phases P_{III} and P_{IV} have the same coverage (0.025 ML), means that both phases adsorb with equal probability on the surface at this potential regime.

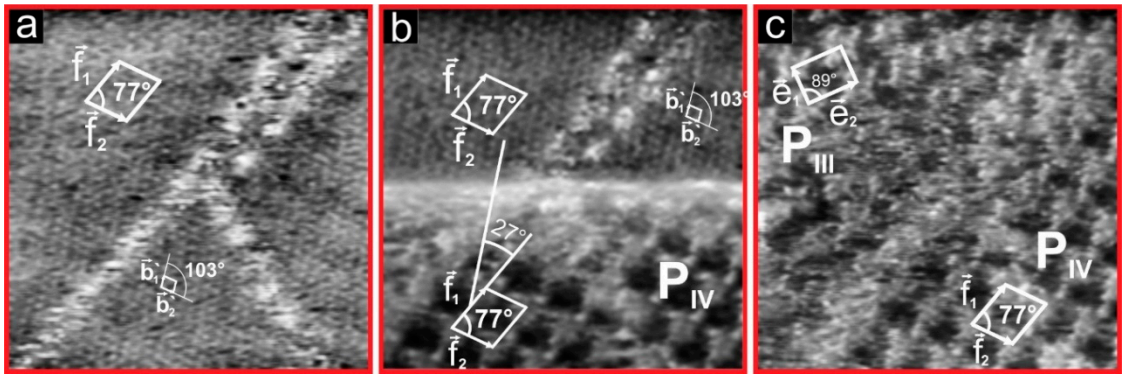

Figure 10. Structure correlation between the H_2TMPyP layer of P_{III} and P_{IV} and the underlying iodine and gold layer, (**a**) Iodine layer underneath at low tunneling bias, 14.12 nm × 14.12 nm, I_t = 1 nA, U_b = −17 mV, E = −200 mV vs. Pt/PtI; (**b**) upper part: Iodine layer underneath at low tunneling bias: U_b = −17 mV, lower part: Porphyrin layer at high tunneling bias: U_b = −472 mV, 14.12 nm × 14.12 nm, I_t = 1 nA, E = −200 mV vs. Pt/PtI; (**c**) Porphyrin layer at high tunneling bias, 14.12 nm × 14.12 nm, I_t = 1 nA, U_b = −472 mV, E = −200 mV vs. Pt/PtI.

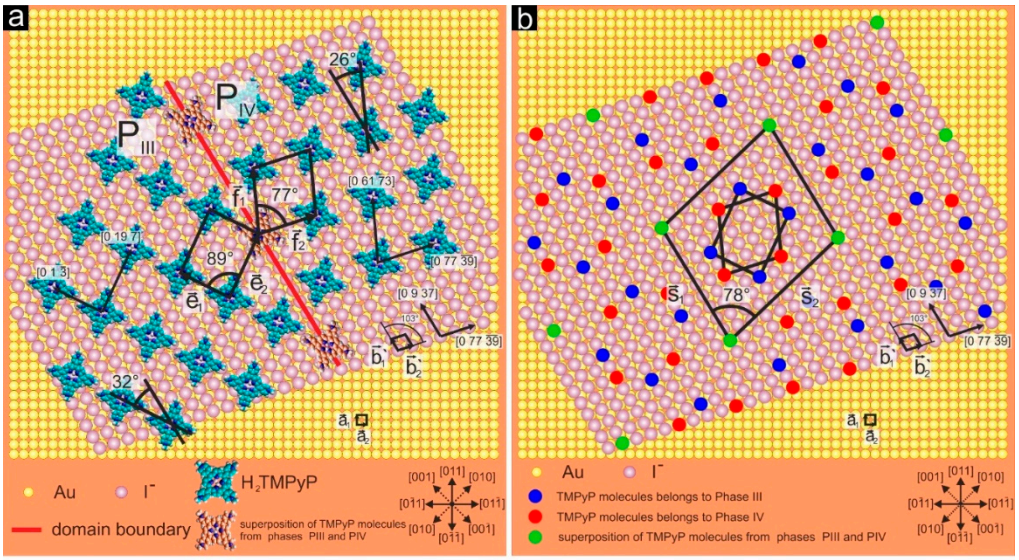

Figure 11. Structural model of P_{III} and P_{IV} on iodine modified Au(100) surface (**a**); structure model of superstructure created by superimposing of Phase III and IV (**b**).

4. Conclusions

In this study, we have investigated in situ the self-assembly of H_2TMPyP molecules on an iodine modified Au(100) electrode surface by EC-STM methods exclusively in the *non-reactive* regime, i.e., in the potential regime in which the molecules retain their oxidized $[H_2TMPyP(0)]^{4+}$ state throughout. The exposure of the *pseudo-hex-rot* iodine modified Au(100) surface to the porphyrin containing solution results in the spontaneous adsorption and lateral ordering of the molecules on the surface, with the organic macrocycles lying flat on the substrate. Up to five different porphyrin phases (P_I–P_V) were detected on the surface of the substrate, whose stabilities, surface concentrations, and existence regimes were demonstrated yet to be potential dependent. In fact, potentio-dynamic STM measurements revealed that P_I and P_{II}, stable structures at more positive potentials, transform into phases P_{III} and P_{IV} by applying more negative electrode potential, while P_V was found to be stable and detected in a very narrow potential window only. Therefore, there is a competition between the different phases, resulting in a strict relationship between their respective surface concentrations and their existence regimes as a function of the applied electrode potential.

In addition, by applying adequate imaging conditions, i.e., bias voltages, STM images were obtained, which enable a correlation between the structures of the porphyrin adlayer and of the underlying iodine and gold lattices. The lattice parameters regarding the relative orientation of the iodine underlayer and the organic overlayer for P_I (at more positive potentials) on the one hand, and for P_{III} and P_{IV} (at more negative potentials) on the other hand were analysed. The results reveal that the observed phase transitions are accompanied by a change of the underlying electro-compressible iodine lattice, in particular, its density, as a function of the electrode potential. Since iodide anions are largely discharged upon adsorption and essentially bound covalently as neutral iodine atoms, it has been suggested in the literature [27,29,30] that porphyrin molecules on iodine modified metal surfaces are predominantly controlled by van der Waals forces. However, our results about potential dependent lattice coincidences and molecular orientations strongly support the notion that not only the van-der-Waals forces are responsible for the self-assembly of the porphyrin molecules on the polarized substrate, but that also electrostatic interactions between the molecules and the iodine modified metal substrate, as well as between the molecules themselves, play a decisive role in the 2D ordering process.

Author Contributions: All authors have made a substantial contribution to the work, and approved it for publication.

Funding: This work has in part been funded by the collaborative research centre 624 of the German Science Foundation.

Acknowledgments: M.B. gratefully acknowledges the Clarin CoFund Program postdoctoral fellowship (ACA17-29), funded by Gobierno del Principado de Asturias and Marie Curie Actions (grant 600196).

Conflicts of Interest: The authors declare no conflict of interest.

References

1. Madueno, R.; Räisänen, M.T.; Silien, C.; Buck, M. Functionalizing hydrogen-bonded surface networks with self-assembled monolayers. *Nature* **2008**, *454*, 618–621. [CrossRef] [PubMed]
2. Li, Z.; Wandlowski, T. Structure formation and annealing of isophthalic acid at the electrochemical Au(111)-electrolyte interface. *J. Phys. Chem. C* **2009**, *113*, 7821–7825. [CrossRef]
3. Barth, J.V.; Weckesser, J.; Lin, N.; Dmitriev, A.; Kern, K. Supramolecular architectures and nanostructures at metal surfaces. *Appl. Phys. A Mater. Sci. Process.* **2003**, *76*, 645–652. [CrossRef]
4. Dmitriev, A.; Lin, N.; Weckesser, J.; Barth, J.V.; Kern, K. Supramolecular assemblies of trimesic acid on a Cu(100) surface. *J. Phys. Chem. B* **2002**, *106*, 6907–6912. [CrossRef]
5. Whitesides, G.M. Self-Assembly at All Scales. *Science* **2002**, *295*, 2418–2421. [CrossRef] [PubMed]
6. Desiraju, G.R. Chemistry beyond the molecule. *Nature* **2001**, *412*, 397–400. [CrossRef] [PubMed]
7. Sosa-Vargas, L.; Kim, E.; Attias, A.J. Beyond "decorative" 2D supramolecular self-assembly: Strategies towards functional surfaces for nanotechnology. *Mater. Horiz.* **2017**, *4*, 570–583. [CrossRef]
8. Safarowsky, C.; Rang, A.; Schalley, C.A.; Wandelt, K.; Broekmann, P. Formation of 2D supramolecular architectures at electrochemical solid/liquid interfaces. *Electrochim. Acta* **2005**, *50*, 4257–4268. [CrossRef]
9. Ciesielski, A.; Palma, C.A.; Bonini, M.; Samori, P. Towards supramolecular engineering of functional nanomaterials: Pre-programming multi-component 2D self-assembly at solid-liquid interfaces. *Adv. Mater.* **2010**, *22*, 3506–3520. [CrossRef] [PubMed]
10. Gottfried, J.M. Surface chemistry of porphyrins and phthalocyanines. *Surf. Sci. Rep.* **2015**, *70*, 259–379. [CrossRef]
11. Hai, N.T.M.; Gasparovic, B.; Wandelt, K.; Broekmann, P. Phase transition in ordered porphyrin layers on iodide modified Cu(111): An EC-STM study. *Surf. Sci.* **2007**, *601*, 2597–2602. [CrossRef]
12. Phan, T.H.; Kosmala, T.; Wandelt, K. Potential dependence of self-assembled porphyrin layers on a Cu(111) electrode surface: In-Situ STM study. *Surf. Sci.* **2015**, *631*, 207–212. [CrossRef]
13. Madry, B.; Morawski, I.; Kosmala, T.; Wandelt, K.; Nowicki, M. Porphyrin Layers at Cu/Au(111)–Electrolyte Interfaces: In Situ EC-STM Study. *Top. Catal.* **2018**, 1–15. [CrossRef]
14. Barth, J.V.; Costantini, G.; Kern, K. Engineering atomic and molecular nanostructures at surfaces. *Nature* **2005**, *437*, 671–679. [CrossRef] [PubMed]
15. Castner, D.G.; Ratner, B.D. Biomedical surface science: Foundations to frontiers. *Surf. Sci.* **2002**, *500*, 28–60. [CrossRef]
16. Lang, K.; Mosinger, J.; Wagnerová, D.M. Photophysical properties of porphyrinoid sensitizers non-covalently bound to host molecules; models for photodynamic therapy. *Coord. Chem. Rev.* **2004**, *248*, 321–350. [CrossRef]
17. Vicente, M.G. Porphyrin-based sensitizers in the detection and treatment of cancer: Recent progress. *Curr. Med. Chem. Anti-Cancer Agents* **2001**, *1*, 175–194. [CrossRef] [PubMed]
18. Lei, J.; Ju, H.; Ikeda, O. Supramolecular assembly of porphyrin bound DNA and its catalytic behavior for nitric oxide reduction. *Electrochim. Acta* **2004**, *49*, 2453–2460. [CrossRef]
19. Ema, T.; Miyazaki, Y.; Shimonishi, J.; Maeda, C.; Hasegawa, J.Y. Bifunctional porphyrin catalysts for the synthesis of cyclic carbonates from epoxides and CO_2: Structural optimization and mechanistic study. *J. Am. Chem. Soc.* **2014**, *136*, 15270–15279. [CrossRef] [PubMed]
20. Purrello, R.; Gurrieri, S.; Lauceri, R. Porphyrin assemblies as chemical sensors. *Coord. Chem. Rev.* **1999**, *190–192*, 683–706. [CrossRef]
21. Hirano, T.; Yui, T.; Okazaki, K.I.; Kajino, T.; Fukushima, Y.; Inoue, H.; Torimoto, T.; Takagi, K. Photo-Induced Electron Migrations in the Nano-Cavities of Mesoporous Silica Sensitized by a Cationic Porphyrin Dye. *J. Nanosci. Nanotechnol.* **2009**, *9*, 495–500. [CrossRef] [PubMed]

22. Lehn, J.-M. Supramolecular Chemistry—Scope and Perspectives Molecules, Supermolecules, and Molecular Devices (Nobel Lecture). *Angew. Chem. Int. Ed. Engl.* **1988**, *27*, 89–112. [CrossRef]
23. Phan, T.H.; Wandelt, K. Molecular self-assembly at metal-electrolyte interfaces. *Int. J. Mol. Sci.* **2013**, *14*, 4498–4524. [CrossRef] [PubMed]
24. Pansu, R.B.; Delmarre, D.; Me, R. Heavy metal ions detection in solution, in sol ± gel and with grafted porphyrin monolayers. *Photochem. Photobiol.* **1999**, *124*, 23–28.
25. He, Y.; Ye, T.; Borguet, E. Porphyrin self-assembly at electrochemical interfaces: Role of potential modulated surface mobility. *J. Am. Chem. Soc.* **2002**, *124*, 11964–11970. [CrossRef] [PubMed]
26. Kunitake, M.; Batina, N.; Itaya, K. Self-Organized Porphyrin Array on Iodine-Modified Au(111) in Electrolyte Solutions: In Situ Scanning Tunneling Microscopy Study. *Langmuir* **1995**, *11*, 2337–2340. [CrossRef]
27. Kunitake, M.; Akiba, U.; Batina, N.; Itaya, K. Structures and dynamic formation processes of porphyrin adlayers on iodine-modified Au(111) in solution: In Situ STM study. *Langmuir* **1997**, *13*, 1607–1615. [CrossRef]
28. Hai, N.T.M. Preparation and characterization of copper-iodide thin films and organic supramolecular layers at copper/electrolyte interfaces. Ph.D. Dissertation, University of Bonn, Bonn, Germany, 2007.
29. Ogaki, K.; Batina, N.; Kunitake, M.; Itaya, K. In Situ Scanning Tunneling Microscopy of Ordering Processes of Adsorbed Porphyrin on Iodine-Modified Ag(111). *J. Phys. Chem.* **1996**, *100*, 7185–7190. [CrossRef]
30. Sashikata, K.; Sugata, T.; Sugimasa, M.; Itaya, K. In Situ Scanning Tunneling Microscopy Observation of a Porphyrin Adlayer on an Iodine-Modified Pt(100) Electrode. *Langmuir* **1998**, *14*, 2896–2902. [CrossRef]
31. Wilms, M.; Kruft, M.; Bermes, G.; Wandelt, K. A new and sophisticated electrochemical scanning tunneling microscope design for the investigation of potentiodynamic processes. *Rev. Sci. Instrum.* **1999**, *70*, 3641. [CrossRef]
32. Gao, X.; Edens, G.J.; Liu, F.-C.; Weaver, M.J.; Hamelin, A. Sensitivity of Electrochemical Adlayer Structure to the Metal Crystallographic Orientation: Potential-Dependent Iodide Adsorption on Au(100) in Comparison with Other Low-Index Surfaces. *J. Phys. Chem.* **1994**, *98*, 8086–8095. [CrossRef]
33. Valenzuela-Benavides, J.; Herrera-Zaldívar, M. Structural transitions of chemisorbed iodine on Au(1 0 0): A STM and LEED study. *Surf. Sci.* **2005**, *592*, 150–158. [CrossRef]
34. Magnussen, O.M. Ordered anion adlayers on metal electrode surfaces. *Chem. Rev.* **2002**, *102*, 679–725. [CrossRef] [PubMed]
35. Su, G.-J.; Zhang, H.-M.; Wan, L.-J.; Bai, C.-L.; Wandlowski, T. Potential-Induced Phase Transition of Trimesic Acid Adlayer on Au(111). *J. Phys. Chem. B* **2004**, *108*, 1931–1937. [CrossRef]
36. Cunha, F.; Jin, Q.; Tao, N.J.; Li, C.-Z. Structural phase transition in self-assembled 1,10′ phenanthroline monolayer on Au(111). *Surf. Sci.* **1997**, *389*, 19–28. [CrossRef]
37. Bai, Y. Photoelectron Spectroscopic Investigations of Porphyrins and Phthalocyanines on Ag(111) and Au (111): Adsorption and Reactivity. Friedrich-Alexander-Universität Erlangen-Nürnberg. 2010. Available online: http://opus4.kobv.de/opus4-fau/frontdoor/deliver/index/docId/1146/file/YunBaiDissertation.pdf (accessed on 13 May 2016).
38. Mizutani, W.; Shigeno, M.; Ono, M.; Kajimura, K. Voltage-dependent scanning tunneling microscopy images of liquid crystals on graphite. *Appl. Phys. Lett.* **1990**, *56*, 1974–1976. [CrossRef]
39. Claypool, C.L.; Faglioni, F.; Goddard, W.A.; Gray, H.B.; Lewis, N.S.; Marcus, R.A. Source of Image Contrast in STM Images of Functionalized Alkanes on Graphite: A Systematic Functional Group Approach. *J. Phys. Chem. B* **1997**, *101*, 5978–5995. [CrossRef]
40. Huemann, S.; Hai, N.T.M.; Broekmann, P.; Wandelt, K.; Zajonz, H.; Dosch, H.; Renner, F. X-ray diffraction and STM study of reactive surfaces under electrochemical control: Cl and I on Cu(100). *J. Phys. Chem. B* **2006**, *110*, 24955–24963. [CrossRef] [PubMed]
41. Röefzaad, M. Ordnungsphänomene redox-aktiver Moleküle auf Elektrodenoberflächen unter reaktiven Bedingungen. Ph.D. Thesis, University of Bonn, Bonn, Germany, 2011.